MULTIBODY DYNAMICS MODEL OF THE CYCLOIDAL GEARBOX, IMPLEMENTED IN FORTRAN FOR ANALYSIS OF DYNAMIC PARAMETERS INFLUENCED BY THE BACKLASH AS A DESIGN TOLERANCE

Roman KRÓL*, Kazimierz KRÓL*

*Faculty of Mechanical Engineering, Department of Applied Mechanics and Mechatronics,
University of Technology and Humanities in Radom, ul. Stasieckiego 54, 26-600 Radom, Poland

r.krol@uthrad.pl, k.krol@uthrad.pl

received 10 October 2022 revised 16 January 2023 accepted 5 February 2023

Abstract: In this study, dynamical parameters of the cycloidal gearbox working at the constant angular velocity of the input shaft were investigated in the multibody dynamics 2D model implemented in the Fortran programming language. Time courses of input and output torques and forces acting on the internal and external sleeves have been shown as a function of the contact modelling parameters and backlash. The analysis results in the model implemented in Fortran were compared with the results in the 3D model designed using MSC Adams software. The values of contact forces are similar in both models. However, in the time courses obtained in MSC Adams there are numerical singularities in the form of peaks reaching 500 N for the forces at external sleeves and 400 N for the forces acting at internal sleeves, whereas in the Fortran model, there are fewer singularities and the maximum values of contact forces at internal and external sleeves do not exceed 200 N. The contact damping and discretisation level (the number of discrete contact points on the cycloidal wheels) significantly affect the accuracy of the results. The accuracy of computations improves when contact damping and discretisation are high. The disadvantage of the high discretization is the extended analysis time. High backlash values lead to a rise in contact forces and a decrease in the force acting time. The model implemented in Fortran gives a fast solution and performs well in the gearbox optimisation process. A reduction of cycloidal wheel discretisation to 600 points, which still allows satisfactory analysis, could reduce the solution time to 4 min, corresponding to an analysis time of 0.6 s with an angular velocity of the input shaft of 52.34 rad/s (500 RPM).

Keywords: cycloidal gearbox, backlash, contact modelling, multibody dynamics, output torque ripple, gearbox efficiency

1. INTRODUCTION

Cycloidal gearboxes find wide application in the drives of robotic systems and the winches of rescue helicopters or off-road vehicles. The cycloidal gearbox design analysed in this study is characterised by the vibration of the output shaft with significant amplitude. The variable angular velocity of the output shaft (Fig. 1) is the source of vibrations, which emerge from the given geometry of the gearbox.

Contemporary research in cycloidal gearbox engineering concerns the construction of discrete models, which contain springs and dampers [1], [2] or modelling of the cycloidal gearbox using engineering software [2], [3]. In the iterative analysis, the current loading state of the cycloidal gearbox depends on previous loading cycles. Excluding back iterations, applying the discrete models for the dynamic analysis gives low-accuracy results. Analysis of the influence of the various contact models on the torque at the output shaft requires constructing transient models based on multibody dynamics. Time courses of the forces and moments obtained in the analysis find their application in developing fault diagnosis methodologies and optimisation. Current research in this area includes fault diagnosis of planetary drives [4–6], while research that concerns cycloidal gearboxes is rare.

Studies in the field of cycloidal gearbox engineering deal with the subject of design issues [7–13], finite element analysis of the cycloidal gearbox parts [7,13–17], kinematical analysis [16,18], applications in robotics [12,16,17,19], friction, lubrication and machining [20–24], measurements [25], efficiency [26,27], optimisation [8,28], contact modelling [29–32], backlash and design tolerances [9,30,33–35] or vibration and dynamics [31,32,36–40].

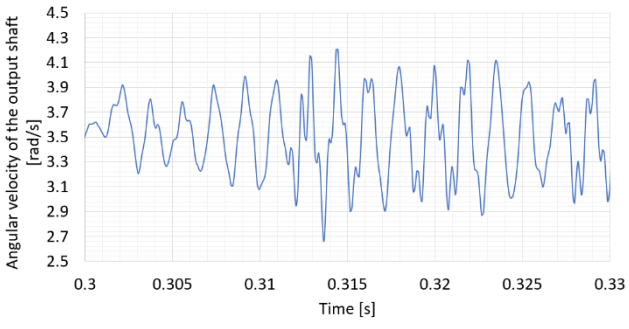

Fig.1. Variable angular velocity of the output shaft

Analysis of the backlash and design tolerances in the cycloidal gearboxes, which deal with the transient analysis, is scarce because it demands programming of the dynamic transient model based on multibody dynamics. Furthermore, high complexity and difficulties in setting up relevant values of the contact modelling parameters (contact damping and contact stiffness, which could

be different for various parts of the gearbox being in contact) in these models allow simplified, static analysis methods to be more attractive.

The motivation to implement the presented transient model was a comprehensive study [32] describing methods of contact modelling in cycloidal gearboxes and showing the time courses of the dynamic entities in the analysed gearbox. The geometry of the cycloidal gearbox presented in Ref [32] is different than that presented in the current article. The difference is also in the adaptive time stepping used in the analysis [32]. The Fortran model described in this article uses the constant time step integrator, simplifying the analysis. Guidelines in contact modelling presented in Ref [32] are a good starting point in programming models of cycloidal gearboxes.

This article describes the transient model [41] programmed in Fortran for fast analysis of the cycloidal gearbox. The possible applications of this model are developing fault diagnosis methods, vibration analysis, contact stress optimisation or analysis of contact models. The authors analysed the backlash in the form of design tolerance, contact stiffness and relative velocity of the contact points in the scope of contact modelling methodology. In addition, the time courses of the forces and moments in the cycloidal gearbox were shown as a function of contact damping.

2. MODELS OF THE CYCLOIDAL GEARBOX

Two models of the cycloidal gearbox were built: the first model was designed using MSC Adams software, and the second model was programmed based on multibody dynamics in Fortran. The second model was also implemented using Matlab software. Unfortunately, the adaptive time step was time-consuming. The version implemented in Fortran, which is a fast structural programming language with computer algebra facilities, uses the 2nd-order Runge Kutta method with constant integration steps. Both models consisted of input and output shafts, two cycloidal wheels and 16 external and eight internal sleeves (Fig. 2). All bodies were mounted on bearings, which allowed relative rotational motions between the parts. The shape of the cycloidal wheels is described in the system of parametric Eq. (1); the parameters from the given system are presented in Tab. 1, the masses and moments of inertia of bodies are given in Tab. 2 and loads are given in Tab. 3.

In the model programmed in Fortran (Fig. 2b), visualisation software (programmed in Java language with the OpenGL library) does not show the input shaft with the eccentric cams on which cycloidal wheels are mounted. The analysed gearbox was designed with the dimensions presented in Fig. 3.

$$\begin{cases} u(\alpha) = \frac{e \cdot z_k}{m}\cos(\alpha) + e \cdot \cos(z_k \cdot \alpha) - q \cdot \cos(\alpha + \gamma) \\ v(\alpha) = \frac{e \cdot z_k}{m}\sin(\alpha) + e \cdot \sin(z_k \cdot \alpha) - q \cdot \sin(\alpha + \gamma) \\ \gamma = \operatorname{atan}\left[\frac{\sin(z_s \cdot \alpha)}{\frac{1}{m} + \cos(z_s \cdot \alpha)}\right] \end{cases}, \quad (1)$$

The input shaft rotates with a constant angular velocity, as given in Tab. 3. The output shaft is loaded by the constant output torque (Tab. 3). Despite the cycloidal gearbox being loaded by a constant output torque, the torque at the output shaft is variable due to the geometry of the gearbox. In Figs. 7b, 15 and 16, the output torque was solved based on the time courses of the forces acting on the internal sleeves and the time courses of the displacements of these sleeves.

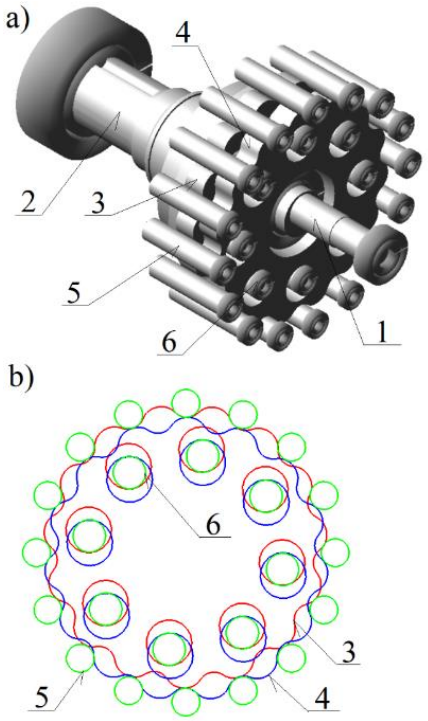

Fig. 2. Cycloidal gearbox models: designed in MSC Adams (a) and programmed in Fortran (b), where: 1 denotes the input shaft, 2 denotes the output shaft, 3 denotes the internal cycloidal wheel, 4 denotes the external cycloidal wheel, 5 denotes the external sleeve, 6 denotes the internal sleeve

Tab. 1. Parameters of the cycloidal wheels defined in parametric Eq. (1)

Parameter	Description	Value
u(α)	Horizontal coordinate	-
v(α)	Vertical coordinate	-
α [rad]	Equation parameter	0-2π
e [m]	Eccentricity	0.0028
z_k	Number of external sleeves	16
z_s	Number of lobes	15
m	Short-width coefficient	0.7
q [m]	Radius of the external sleeve	0.006

Tab. 2. Masses and moments of inertia relative to the local coordinate systems. The local coordinate systems are placed in the parts' centre of gravity. The parts are rigid bodies

Body	Model parameters	
	Mass [kg]	Moment of inertia [kg·m²]
Input shaft	0.2341	$1.846 \cdot 10^{-6}$
Output shaft	1.6345	$1.373 \cdot 10^{-4}$
Cycloidal wheel	0.5998	$1.57538 \cdot 10^{-4}$
Internal sleeve	0.048	$1.1013 \cdot 10^{-5}$
External sleeve	0.048	$1.1013 \cdot 10^{-5}$

Tab. 3. Loads and excitations in the models

Entity	Value
Angular velocity of the input shaft [Hz; rad/s; RPM]	8.33; 52.34; 500
Torque applied at the output shaft [Nm]	22

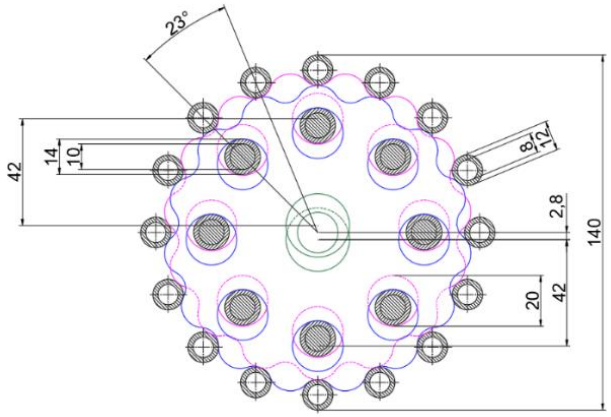

Fig. 3. Dimensions of the cycloidal gearbox analysed using MSC Adams and the model programmed in Fortran

3. MULTIBODY DYNAMICS METHODS USED IN THE MODEL PROGRAMMED IN FORTRAN

The following system of Eq. (2) is solved in each integration subroutine step. The model contains 28 bodies and 29 joints, one of which is a driver joint and the others are revolute joints. The joints appear in the system of Eq. (2) as constraint equations, which are components of the Jacobian matrix. The method of Jacobian matrix formulation is described in [42], [43].

$$\begin{bmatrix} M & -D^T \\ D & 0 \end{bmatrix} \begin{bmatrix} \ddot{u} \\ \lambda \end{bmatrix} = \begin{bmatrix} F \\ \gamma \end{bmatrix}, \tag{2}$$

where M is the mass matrix (contains masses and moments of inertia of the parts), D is the Jacobian matrix, 0 is the zero matrix, $\ddot{u}$ denotes solved accelerations, λ denotes solved reaction forces, F is the vector of applied forces and moments and γ is the right-hand side vector of the acceleration equations.

In the described model, the body-coordinate formulation was used. The constraint equations for the revolute joint and the drive joint are given in Eqs. (3) and (4), respectively. The Jacobian matrix satisfies (5), where the components of this matrix depend on the type of joint. Submatrices of the Jacobian matrix for the revolute joint are given in Eqs. (6) and (7) and those of the driver joint in Eq. (8).

$$\Phi_{rev} = r_{P1} - r_{P2} = 0, \tag{3}$$

where Φ_{rev} is the revolute joint constraint equation and r_{P1} and r_{P2} are the position vector of the revolute joint attachment point on the 1st and the 2nd body, respectively. The position vectors are given in the global coordinate system.

$$\Phi_{driver} = \varphi - f(t) = 0, \tag{4}$$

where Φ_{driver} is the driver joint constraint equation, φ is the initial angle of a relative rotation of the connected parts and f(t) is the time course of the rotation angle between the connected parts (i.e. f(t)=ωt for the simulation of the motion with the constant angular velocity ω).

$$D = \frac{\partial \Phi}{\partial u}, \tag{5}$$

where D is the Jacobian matrix, Φ is the constraint equation and u is the vector of body coordinates.

$$D_1 = \begin{bmatrix} -1 & 0 & -\check{s}_{1X} \\ 0 & -1 & -\check{s}_{1Y} \end{bmatrix}, \tag{6}$$

$$D_2 = \begin{bmatrix} 1 & 0 & \check{s}_{2X} \\ 0 & 1 & \check{s}_{2Y} \end{bmatrix}, \tag{7}$$

where D1 and D2 are the Jacobian submatrix corresponding to the 1st and the 2nd body connected to the revolute joint, respectively; $\check{s}$ is the vector orthogonal to the joint attachment point local vector, relative to the centre of mass and X and Y are coordinates of the orthogonal vector.

$$D_{\mathrm{drv}} = [0 \quad 0 \quad 1], \tag{8}$$

where D_{drv} is the Jacobian submatrix corresponding to the driven body. The right-hand side acceleration equations vector contains 0 in the components corresponding to the driver-joint. For the revolute joint, the right-hand side acceleration vector is solved according to Eq. (9).

$$\gamma = \dot{\check{s}}_1 \dot{\phi}_1 - \dot{\check{s}}_2 \dot{\phi}_2, \tag{9}$$

where $\dot{\phi}_1$ and $\dot{\phi}_2$ are angular velocities of the 1st and the 2nd body attached to the revolute joint.

4. CONTACT MODELLING

Methods presented in the previous chapter were used to model three groups of parts in the cycloidal gearbox: (1) the input shaft with cycloidal wheels, (2) the output shaft with internal sleeves and (3) external sleeves. The gearbox should transfer the moment from the input shaft to the output shaft. Therefore contact should be set between mentioned parts. The Kelvin Voigt contact model based on the Hertzian theory with energy dissipation was programmed in four subroutines, which check the contact between two cycloidal wheels, external sleeves and internal sleeves. Subroutines that control the contact between the cycloidal wheels and the external sleeves solve the cycloidal wheel curvature in the contact point based on circular approximation from the three neighbouring points. Subroutines that check the contact between the cycloidal wheels and the internal sleeves use a constant stiffness coefficient because contact surfaces have a constant curvature radius.

Cycloidal wheels and their holes were discretised in the contact checking subroutines. The contact points on the cycloidal wheel boundary (Fig. 4) are placed with the constant angular increment α in Eq. (1). Convergence was obtained for 600 (rough analysis) and 4,000 (refined analysis) points in each cycloidal wheel and 20 (rough analysis) and 100 (refined analysis) in the cycloidal wheel holes in which the internal sleeves occur.

In the contact checking subroutine, the list of points is created whose distance to the centre of the sleeve is less than the sleeve's radius. The subroutine selects the point closest to the sleeve centre from the list of points being in contact. Two points, W and Q, detected by the contact checking subroutine are shown in Fig. 4.

Given the external sleeve centre of mass coordinates and point W (Fig. 4) coordinates, the contact normal vector is computed according to Eq. (10):

$$\vec{\boldsymbol{n}} = [W_x - P_{nX}, W_y - P_{nY}], \tag{10}$$

where W_X and W_Y are coordinates of the selected cycloidal wheel point being in contact with the external sleeve and P_{nX} and P_{nY} are

coordinates of the given external sleeve centre of mass. To solve the friction force, the tangent contact vector (11) is solved using the rotation matrix R_{90} (12):

$$\vec{t} = R_{90} \cdot \|\vec{n}\|, \tag{11}$$

$$R_{90} = \begin{bmatrix} \cos(90°) & -\sin(90°) \\ \sin(90°) & \cos(90°) \end{bmatrix}, \tag{12}$$

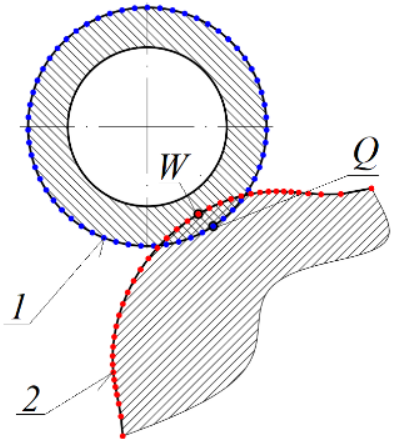

Fig. 4. Two points, W and Q, detected by the contact checking subroutine. 1 denotes the external sleeve, 2 denotes the cycloidal wheel, Q is a point on the external sleeve and W is a point on the cycloidal wheel

The vector r_{pQ} of the contact point Q position relative to the global coordinate system can be computed using Eq. (13). The linear velocity $\dot{r}_{cW}$ of the point W can be computed using Eq. (14) with the cycloidal wheel rotation matrix specified in Eq. (15):

$$r_{pQ} = r_p + R_{exsl} \cdot \|\vec{n}\|, \tag{13}$$

$$\dot{r}_{cW} = \dot{r}_c + \dot{A}_c \cdot s_{cW}, \tag{14}$$

$$A_c = \begin{bmatrix} \cos(\varphi_c) & -\sin(\varphi_c) \\ \sin(\varphi_c) & \cos(\varphi_c) \end{bmatrix}, \tag{15}$$

where r_p is the vector of the external sleeves' centre of mass localisation relative to the global coordinate system, R_{exsl} is the radius of the external sleeve, $\|\vec{n}\|$ is the contact normal vector with normalised length, A_C is the rotation matrix of the cycloidal wheel, φ_c is the angle of cycloidal wheel rotation, s_{cW} is the local vector of the contact point W position relative to the cycloidal wheel centre of mass and $\dot{r}_c$ is the linear velocity vector of the cycloidal wheels' centre of mass.

The normalised contact normal velocity is given in Eq. (16). The linear velocity (17) of the Q point can be computed by differentiating Eq. (13) and substituting Eq. (16). Contact normal velocity and contact tangential velocity can be solved using Eqs. (18) and (19) based on Eqs. (10), (11), (14) and (17):

$$\|\dot{\vec{n}}\| = \dot{r}_{cW} - \dot{r}_p, \tag{16}$$

$$\dot{r}_{pQ} = \dot{r}_p + R_{exsl} \cdot \|\dot{\vec{n}}\|, \tag{17}$$

$$v_n = (\dot{r}_{pQ} - \dot{r}_{cW}) \cdot \|\vec{n}\|, \tag{18}$$

$$v_t = (\dot{r}_{pQ} - \dot{r}_{cW}) \cdot \|\vec{t}\|, \tag{19}$$

where v_n is the contact normal velocity and v_t is the contact tangential velocity. The theory that concerns velocity computation is discussed in detail in Refs [32], [44].

The contact normal velocity is used for the computation of the contact normal force (20), and the contact tangential velocity is used to compute the friction force (21). Contact normal force can be computed using various methods presented in Ref [44]. In the Fortran model, the models of Lee and Wang or Herbert and McWhannel [44] were implemented. Unfortunately, the convergence was not obtained for the specified models designed for sphere-to-sphere contact and using initial contact velocity. Instead, the approach from MSC Adams documentation [45], [46] was used, and the Heaviside function was utilised in the modelling of the contact stiffness and contact damping (20). The Heaviside function S(t-t0) (22) is linear from 0 to t0.

$$F_n = S(\delta - 0.00001) \cdot K \cdot \delta^{1.5} + S(\delta - 0.00001) \cdot C \cdot v_n, \tag{20}$$

$$F_t = -\mu \cdot S(v_t - 0.00005) \cdot F_n, \tag{21}$$

where S is the Heaviside step function (22), K denotes contact stiffness, C denotes contact damping, v_n is the contact normal velocity, v_t is the contact tangential velocity, μ is the static coefficient of friction and δ is the penetration depth (the distance between W and Q points):

$$S(t - t_0) = \begin{cases} 0 \; for \; t < 0 \\ \frac{1}{t_0} \cdot t \; for \; t \in (0, t_0). \\ 1 \; for \; t > t_0 \end{cases} \tag{22}$$

The stiffness coefficient (23) [32], [44] is solved based on the surface curvature of the contacting bodies and the parameters given in Eq. (24). The contact stiffness coefficient was multiplied by the H multiplier. The values of the H multiplier and contact damping C are presented in Tab. 4.

$$K = \frac{4H}{3\pi(h_c + h_p)} \sqrt{\frac{R_c \cdot R_p}{R_c \pm R_p}}, \tag{23}$$

$$h_c = \frac{1 - \nu_c^2}{\pi \cdot E_c}, h_p = \frac{1 - \nu_p^2}{\pi \cdot E_p}, \tag{24}$$

where K denotes contact stiffness; H is the contact stiffness multiplier; R_c is the radius of curvature of the cycloidal wheel surface; R_p is the radius of curvature of the external sleeve surface; ν_c and ν_p are Poisson ratios of the cycloidal wheel and the external sleeve material, respectively; and E_c and E_p are Young moduli of the cycloidal wheel and the external sleeve, respectively. The sign in the denominator between R_c and R_p values depends on the contact with the cycloidal wheel pit or the cycloidal wheel lobe (the negative or positive radius of curvature of the cycloidal wheel).

Tab. 4. Parameters used in contact modelling

Parameter	Values used by contact detection subroutines (external and internal sleeves)
ν_c, ν_p	0.3
E_c, E_p [N/m^2]	$2 \cdot 10^{11}$
C [Ns/m]	8
H	0.01

Computed values of the forces and moments acting on the external sleeves, internal sleeves and cycloidal wheels are substi-

tuted to the system of Eq. (2) in the F vector in each iteration of the 2nd order Runge Kutta algorithm. In the solution process, the constant integration step was used with 10^{-5} s. The analysis time was set to 0.6 s.

5. RESULTS OF THE ANALYSIS IN THE FORTRAN MODEL

One of the benefits of the transient model programmed in Fortran is the possibility to analyse a graph of every entity in the simulation process. MSC Adams allows the user to enter a constant value of the contact stiffness. In the Fortran model, the value of the contact stiffness depends on the curvature of contacting bodies at the point of contact. Contact stiffness at the moment of contact between the cycloidal wheel and one of the external sleeves is shown in Fig. 5. In Fig. 6 the relative velocity of the contact points is shown at the time of contact with the same sleeve. Figs. 5 and 6 show periodically changing values of contact stiffness and relative velocity, which can differ in detail for the following periods. These differences arise from the numerical solution process and its inaccuracies. The mentioned entities have been shown in the time range when the contact between the external sleeve and the cycloidal wheel is active. In the rest of the period, the parts do not interfere with each other.

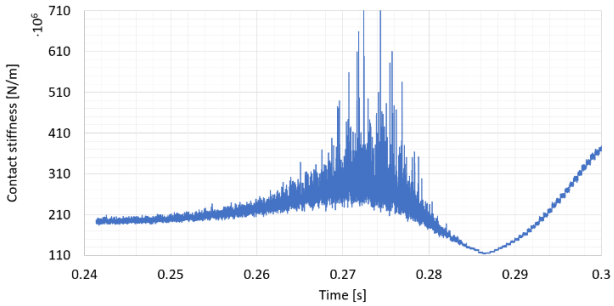

Fig. 5. Contact stiffness in the time range, when contact between the external sleeve and cycloidal wheel occurs. Analysis without backlash

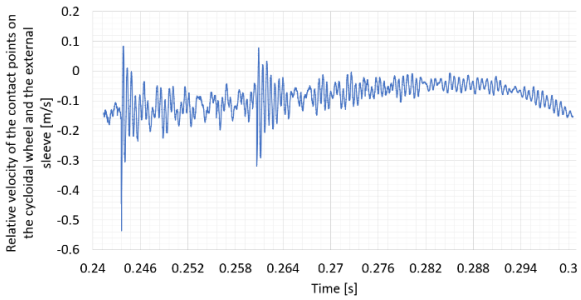

Fig. 6. Relative velocity of the contact points on the cycloidal wheel and the external sleeve. Analysis without backlash

Time courses of the input torque and output torque are shown in Figs. 7a and 7b respectively. It can be seen that despite the cycloidal gearbox being loaded by the constant output torque, the courses of the input and output torques oscillate due to the geometry. Forces acting on the internal and external sleeves are shown in Figs. 8a and 8b, respectively. Figs. 7 and 8 depict time courses of the dynamical entities for different values of the contact damping. This parameter significantly influences the accuracy of results. The presented time courses oscillate with high amplitude for low contact damping values. Structural damping for steel is considered to be less than 0.01 of the critical damping. The presented analysis modelled contact as the Kelvin Voigt model with spring and damper (viscous damping). For accurate contact modelling in the numerical analysis, according to Ref [46], the damping should be set to one per cent of the contact stiffness coefficient (23).

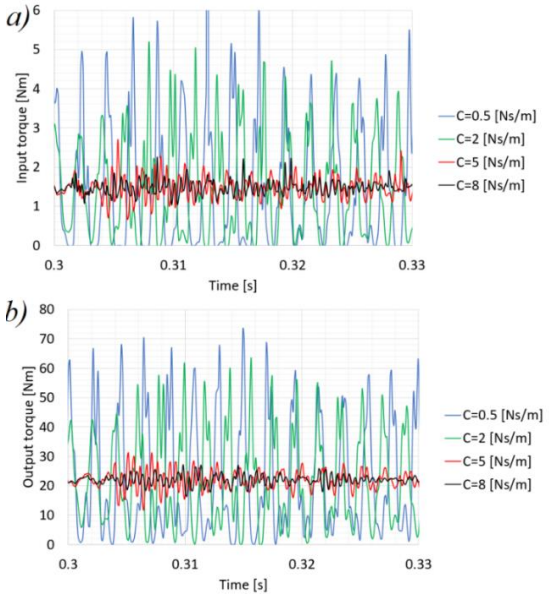

Fig. 7. Physical entities computed in the model programmed in Fortran: torque at the input shaft (a), torque at the output shaft (b)

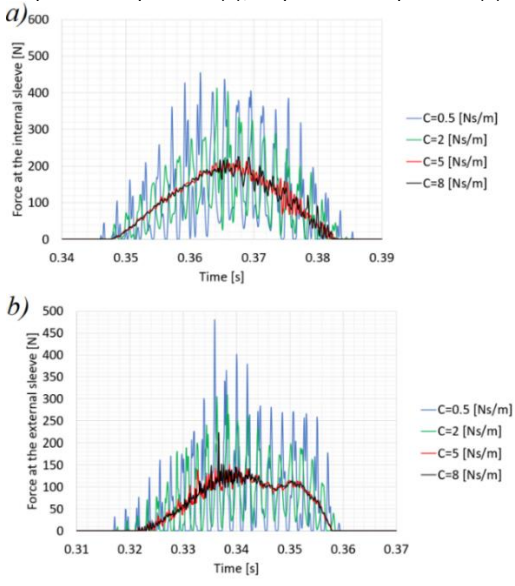

Fig. 8. Physical entities computed in the model programmed in Fortran: the force acting on the internal sleeve (magnitude) (a), the force acting on the external sleeve (magnitude) (b)

In the analysis presented in the current article, an increase in the contact damping above 8 Ns/m leads to non-convergence. The choice of the specified damping factor is motivated by the methodology of the contact modelling and is not related to the specific material.

Fig. 9 (a, b) presents a comparison of the force acting on the internal sleeve and the external sleeve obtained with rough dis-

DOI 10.2478/ama-2023-0031

cretisation (600 points for each cycloidal wheel) and refined analysis (4,000 points for each cycloidal wheel). The results obtained in MSC Adams were compared with the results from the transient model programmed in Fortran in Fig. 10 (a, b).

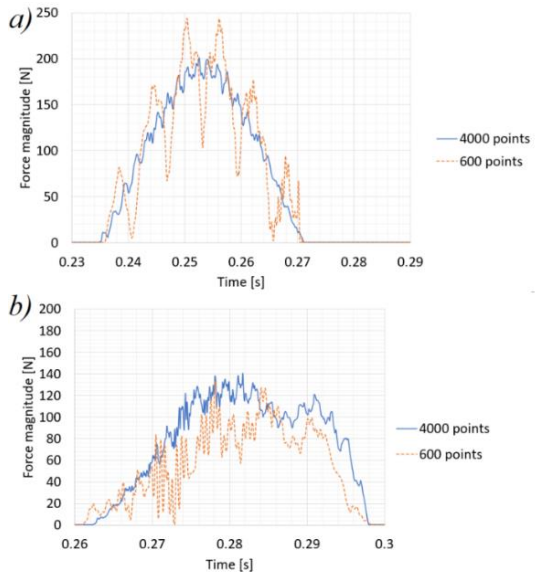

Fig. 9. Results computed in the model implemented in Fortran for various numbers of points in the cycloidal wheel (600 points and 4000 points): force acting on the internal sleeve (magnitude) (a), force acting on the external sleeve (magnitude) (b)

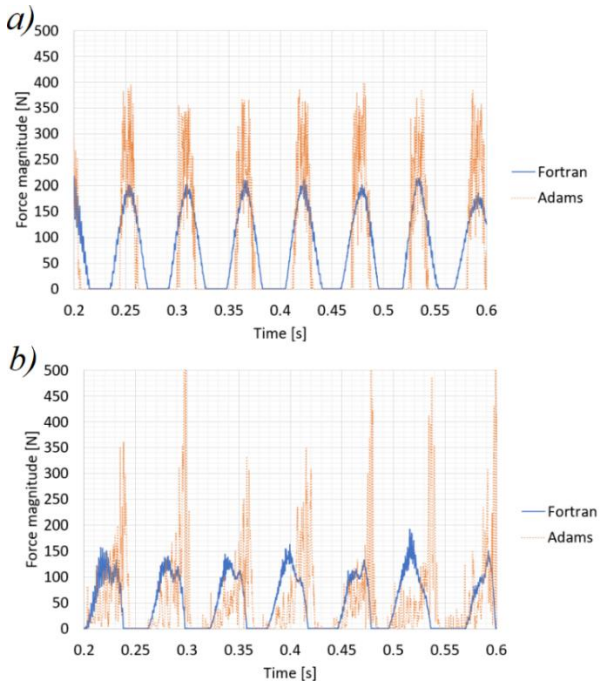

Fig. 10. Results from MSC Adams and the model implemented in Fortran: force acting on the internal sleeve (magnitude) (a) and force acting on the external sleeve (magnitude) (b)

6. BACKLASH INFLUENCE ON THE DYNAMIC PARAMETERS OF THE CYCLOIDAL GEARBOX

Analysis of backlash was performed in the model implemented in Fortran. In the analysed cycloidal gearbox, the artificial backlash was introduced in the form of design tolerance. The design tolerance value *d* increased the external sleeves' radial position. In the analysis without backlash, the radius of their localisation is *r*. After the introduction of backlash, it is *r*+*d* (Fig. 11).

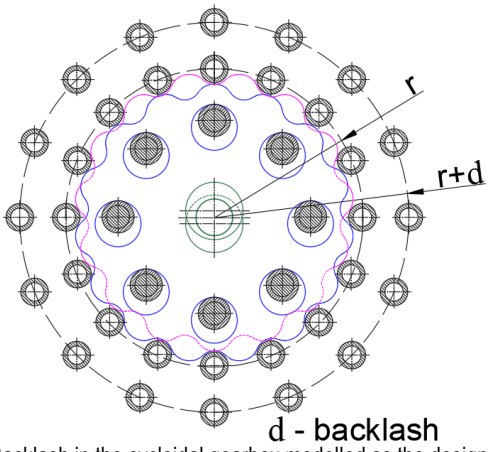

Fig. 11. Backlash in the cycloidal gearbox modelled as the design tolerance d of the radial position r of the external sleeves

The backlash has a decisive impact on the dynamic entities of the cycloidal gearbox (forces acting on the sleeves and torques at the shafts). An increase in backlash significantly influences the force at the external sleeve during cycloidal gearbox work. The higher the backlash, the shorter the contact duration between the external sleeve and the cycloidal wheel. High backlash ($0.6 \cdot 10^{-3}$ m) can increase the force magnitude by 50% relative to the force in the model without backlash (Fig. 12).

There is less influence of the backlash on the value of the force acting on the internal sleeve. However, for the high backlash, a higher amplitude of the force at the internal sleeve oscillations can temporarily arise (Fig. 13).

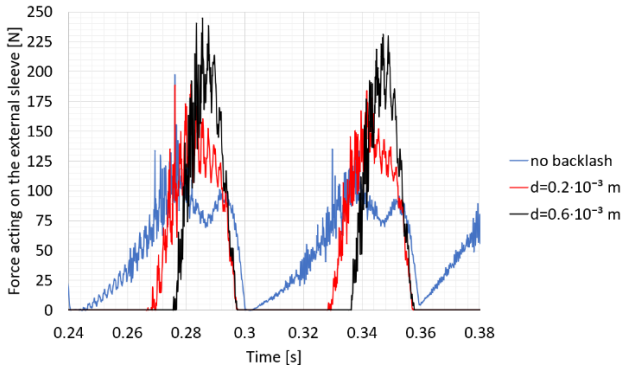

Fig. 12. Contact forces acting on the external sleeves as a function of backlash

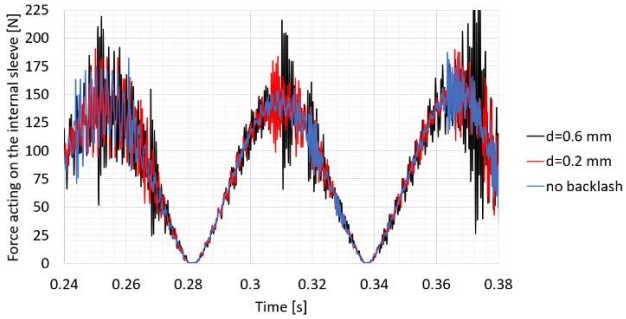

Fig. 13. Contact forces acting on the internal sleeves as a function of backlash

High backlash is unwanted in robotics applications, where reducing the amplitude of oscillations is desirable. Figs. 14 and 15 show an increase in the amplitude of the vibrations for the models with backlash. As mentioned before, in the cycloidal gearbox, the output torque's current state depends on the previous iterations of the analysis. Therefore, the output torque can significantly change its amplitude of oscillations in time. Figs. 14 and 15 present that the amplitude of the vibrations in the analysis without backlash is considerably lower than that with backlash, in general. Fig. 16 shows a higher range of the time in the torque at the output shaft. The torques shown in Figs. 14-16 are random time functions with an unpredictable amplitude, which does not reach a steady state.

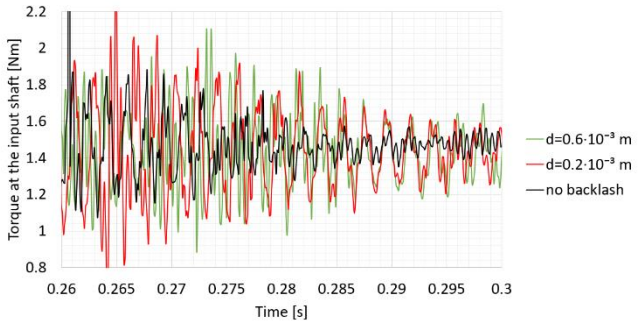

Fig. 14. Torque at the input shaft as a function of backlash

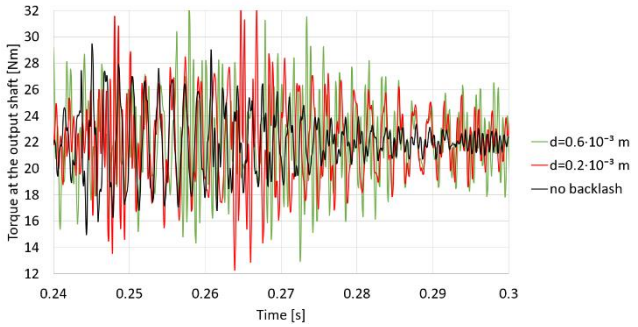

Fig. 15. Torque at the output shaft as a function of backlash

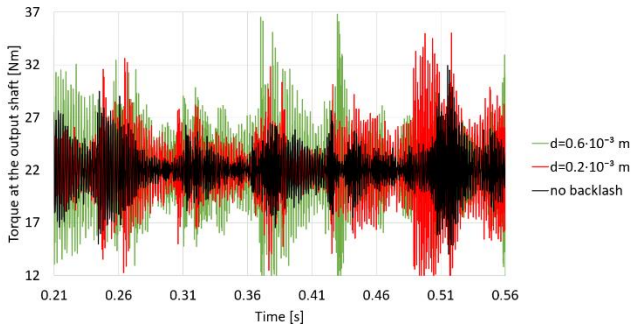

Fig. 16. Torque at the output shaft as a function of backlash. Over a wider time range, the function was shown to be random

In Fig. 17, the time courses of the contact stiffnesses are shown for various backlash values. For various backlashes, multiple shifts in time of the contact stiffness are obtained. It is related to the contact periods between the external sleeve and the cycloidal wheel.

Relative velocities of the contact points (Fig. 4, points W and Q) for various values of backlash are shown in Fig. 18. For each relative velocity, its time course starts with oscillations. However, the time courses for the multiple backlashes overlap in the corresponding time ranges. It shows that for high backlash, the contact between the cycloidal wheel and the external sleeve starts with a higher velocity, which leads to a higher impact and higher value of contact force (Fig. 12).

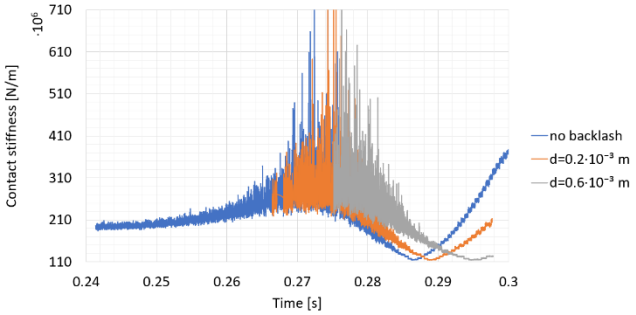

Fig. 17. Contact stiffness between the cycloidal wheel and the external sleeves as a function of backlash

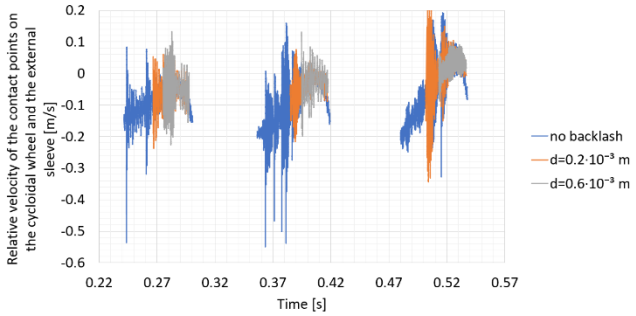

Fig. 18. Relative velocity of the contact points on the cycloidal wheel and the external sleeve as a function of backlash

7. DISCUSSION OF RESULTS

The presented model implemented in Fortran offers a short analysis time, which allows using this model in the optimisation processes. For rough discretisation, the solution time is 4 min, while for refined analysis it is 25 min. Analysis results from MSC Adams presented in Fig. 10 (a, b) require more than 1 h for the solution process.

In the model implemented in Fortran, various contact force models [44] were tested, but convergence was not obtained. These models were designed for two contacting spheres, while the contact in the analysed cycloidal gearbox is cylinder to cylinder. Therefore, the contact stiffness solved according to the Hertzian model should be multiplied by the coefficient H=0.01 to satisfy convergence conditions.

Analysis of various damping coefficients (Figs. 7 and 8) shows that contact damping significantly influences the quality of results. High oscillations emerge for low contact damping values, while more increased contact damping values guarantee smooth results. The MSC Adams results presented in Fig. 10 (a, b) show significant oscillations in the force diagrams for the internal and external sleeves. It can arise from the improper value of the contact damping coefficient, which was set to the same value in the model implemented in Fortran. Analysis of the 3D model in MSC Adams requires another set of contact parameters (contact stiff-

ness, contact damping and the penetration depth at which the contact damping coefficient reaches maximum value).

The model implemented in Fortran can be used in the optimisation process. Therefore it is beneficial to reduce the solution time of the single simulation. Unfortunately, Fig. 9 (a, b) presents that application of the discretisation, which is too rough leads to inaccurate results. The results for the 600 points of discretisation show significant oscillations of the force acting on the internal sleeve in Fig. 9a. The level of discretisation depends on the optimisation demand.

The model programmed in Fortran allows for a more straightforward geometry parametrisation. It is much easier to modify the design tolerances of the model programmed in Fortran than to modify those in the engineering software (MSC Adams). Backlash introduced as the design tolerance of the position of the external sleeves has more impact on the forces acting on the external than on the internal sleeves. Time courses of the force acting on the internal sleeve in Fig. 13 for the high values of backlash have short-in-time oscillations at the peak values of force, which can be 25% higher than peak values in the analysis without backlash.

High backlash is unwanted in applications where the vibrations should be reduced. With increased backlash, the cycloidal wheel comes into contact with the external sleeve with a higher velocity (Fig. 18), which leads to more significant impacts and an increase in the values of contact forces. In addition, higher effects on the external sleeves lead to more remarkable changes in the dynamic parameters of the cycloidal gearbox, which in turn lead to higher oscillations of the input and output torques (Figs. 14 and 15).

Multibody dynamics models provide more accurate results than static calculations or discrete models. Unfortunately, these models contain drawbacks of numerical analyses. At the initial stage correction of the initial parameters is performed. However, the rise of external forces at the first iteration of the simulation leads to disruption of the results. The beginning part of the time course of almost every entity in this model is noised. In the other part of the analysis, the model undergoes stabilisation, and the results are more accurate. It is also an issue in using a proper contact model, including contact stiffness and contact damping solution. Rapid changes in external forces occur at the beginning of the contact between the cycloidal wheel and the external sleeve. On the time courses of relative contact velocity or contact stiffness, oscillations with high amplitude can be seen. Fig. 6 presents fluctuations in the range of 0.24-0.246 s at the beginning of the contact. The oscillations can also appear in the rapid changes of the curvature of the contacting bodies (Fig. 5, period 0.265-0.28 s), which is additionally influenced by the discretisation of the cycloidal wheel.

8. CONCLUSIONS

Summing up the results, the model implemented in Fortran guarantees a fast solution and can be successfully used in the optimisation process. The discretisation of the model should be considered when the accuracy of the optimization results is an essential factor. The contact stiffness should be multiplied by the experimentally adjusted coefficient to allow convergence of the solution process. The contact damping coefficient can significantly influence the accuracy of the results. The backlash has an essential impact on contact forces.

The main drawback of the numerical multibody dynamics analyses is oscillations, which could be caused by the initial rapid changes in the model parameters, discretisation and contact modelling methods.

REFERENCES

1. Wikło M, Król R, Olejarczyk K, Kołodziejczyk K. Output torque ripple for a cycloidal gear train. Proc Inst Mech Eng C J Mech Eng Sci 2019;233:7270–81. https://doi.org/10.1177/0954406219841656.
2. Król R. Resonance phenomenon in the single stage cycloidal gearbox. Analysis of vibrations at the output shaft as a function of the external sleeves stiffness. Archive of Mechanical Engineering 2021;68:303–20. https://doi.org/10.24425/ame.2021.137050.
3. Król R. Kinematics and dynamics of the two stage cycloidal gearbox. AUTOBUSY – Technika, Eksploatacja, Systemy Transportowe 2018;19:523–7. https://doi.org/10.24136/atest.2018.125.
4. Plöger DF, Zech P, Rinderknecht S. Vibration signature analysis of commodity planetary gearboxes. Mech Syst Signal Process 2019;119:255–65. https://doi.org/10.1016/j.ymssp.2018.09.014.
5. Lei Y, Han D, Lin J, He Z. Planetary gearbox fault diagnosis using an adaptive stochastic resonance method. Mech Syst Signal Process 2013;38:113–24. https://doi.org/10.1016/j.ymssp.2012.06.021.
6. Wang T, Han Q, Chu F, Feng Z. Vibration based condition monitoring and fault diagnosis of wind turbine planetary gearbox: A review. Mech Syst Signal Process 2019;126:662–85. https://doi.org/10.1016/j.ymssp.2019.02.051.
7. Naveen P, Kiran R, Siva Sankaram EVS, Bha-radwaj TM. Design, Analysis and Simulation of Compact Cycloidal Drive. Int J Sci Res Sci Eng Technol 2020;7:216–20. https://doi.org/10.32628/ijsrset207547.
8. Król R, Król K. Optymalizacja nieliniowa przekładni cykloidalnej z ograniczeniami równościowymi na wymiary obudowy. In: Pawliczek R, Owsinski R, Łagoda T, editors. Projektowanie, budowa i eksploatacja maszyn cz. 1, vol. 558, Opole: Politechnika Opolska; 2021, p. 95–108.
9. Li T, An X, Deng X, Li J, Li Y. A new tooth profile modification method of cycloidal gears in precision reducers for robots. Applied Sciences 2020;10. https://doi.org/10.3390/app10041266.
10. Kormin TG, Tsumbu JDB. Cycloidal reducer with rotation external ring gear. IOP Conf Ser Mater Sci Eng 2020;971. https://doi.org/10.1088/1757-899X/971/4/042072.
11. Huang X, Zhang J. Analysis of Geometric Characteristics of Cycloidal Transmission. IOP Conf Ser Mater Sci Eng 2020;751:12059. https://doi.org/10.1088/1757-899X/751/1/012059.
12. Huang JT, Li CW. The High-payload Manipulator Development Based on Novel Two-stage Cycloidal Speed Reducers and Hub Motors. J Phys Conf Ser 2020;1583:12002. https://doi.org/10.1088/1742-6596/1583/1/012002.
13. Blagojevic M, Marjanovic N, Djordjevic Z, Stojanovic B, Disic A. A new design of a two-stage cycloidal speed reducer. Journal of Mechanical Design 2011;133. https://doi.org/10.1115/1.4004540.
14. Olejarczyk K, Wiklo M, Król K, Kolodziejczyk K. Cycloidal disc calculation of cycloidal gear using finite element method. Logistyka 2015;6.
15. Blagojevic M, Marjanovic N, Stojanovic B, Blagojević M, Marjanović N, Đorđević Z. Stress And Strain State Of Single-Stage Cy-Cloidal Speed Reducer. The 7th International Conference Research And Development Of Mechanical Elements And Systems Irmes, 2011.
16. Strutynskyi S, Semenchuk R. Investigation of the accuracy of the manipulator of the robotic complex constructed on the basis of cycloidal transmission. Technology Audit and Production Reserves 2021;4:6–14. https://doi.org/10.15587/2706-5448.2021.237326.
17. Chavan U, Joshi A, Kolambe Y, Gwalani H, Chaudhari H, Khalate A, et al. Magnification of energy transmission ratio using miniature cycloidal gear box for humanoids. IOP Conf Ser Mater Sci Eng 2022;1272:012017. https://doi.org/10.1088/1757-899X/1272/1/012017.

18. Blagojevic M, Pantić I, Blagojević M. KINEMATIC ANALYSIS OF SINGLESTAGE CYCLOIDAL SPEED REDUCER. Machine Design 2015;7:113–8.
19. Al Kouzbary M, Al Kouzbary H, Liu J, Khamis T, Al-Hashimi Z, Shasmin HN, et al. Robotic Knee Prosthesis with Cycloidal Gear and Four-Bar Mechanism Optimized Using Particle Swarm Algorithm. Actuators 2022;11. https://doi.org/10.3390/act11090253.
20. Tonoli A, Amati N, Impinna F, Detoni G, Ruzimov S, Gasparin E, et al. Influence of dry friction on the irreversibility of cycloidal speed reducer. 5th World Tribology Congress, WTC 2013, 2013.
21. Luo SM, Liao LX, Mo JY. Prediction of surface roughness of end milling for cycloidal gears based on orthogonal tests. Engineering Transactions 2018;66:339–52. https://doi.org/10.24423/EngTrans.860.20180830.
22. Blagojevic M, Marjanovic N, Stojanovic B, Ivanovic L. Influence of the friction on the cycloidal speed reducer efficiency. Journal of the Balkan Tribological Association 2012;18:217–27.
23. Bo W, Jiaxu W, Guangwu Z, Rongsong Y, Hongjun Z, Tao H. Mixed lubrication analysis of modified cycloidal gear used in the RV reducer. Proceedings of the Institution of Mechanical Engineers, Part J: Journal of Engineering Tribology 2016;230:121–34. https://doi.org/10.1177/1350650115593301.
24. Vasić M, Blagojević M, Dragoi M. Thermal stability of lubricants in cycloidal reducers. Engineering Today 2022;1:7–17. https://doi.org/10.5937/engtoday2202007v.
25. Zaręba R, Mazur T, Olejarczyk K, Bzinkowski D. Measurement of the Cycloidal Drive Sleeves and Pins. Mechanika 2021;27:505–12. https://doi.org/10.5755/J02.MECH.27815.
26. Petrovskiy AN. Increased efficiency of eccentric cycloidal engagement. Proceedings of Higher Educational Institutions Machine Building 2021:3–14. https://doi.org/10.18698/0536-1044-2021-9-3-14.
27. Olejarczyk K, Wikło M, Kołodziejczyk K, Król R, Król K. Theoretical and experimental verification of one stage cycloidal gearbox efficiency. Advances in Mechanism and Machine Science, vol. 73, Springer Science and Business Media B.V.; 2019, p. 1029–38. https://doi.org/10.1007/978-3-030-20131-9_102.
28. Król R, Wikło M, Olejarczyk K, Kołodziejczyk K, Zieja A. Optimization of the one stage cycloidal gearbox as a non-linear least squares problem. Advances in Mechanism and Machine Science, 2019, p. 1039–48. https://doi.org/10.1007/978-3-030-20131-9_103.
29. Sun X, Han L, Wang J. Tooth modification and loaded tooth contact analysis of China Bearing Reducer. Proc Inst Mech Eng C J Mech Eng Sci 2019;233:6240–61. https://doi.org/10.1177/0954406219858184.
30. Li T, Wang G, Deng X, An X, Xing C, Ma W. Contact Analysis of Cycloidal-pin Gear of RV Reducer under the Influence of Profile Error. J Phys Conf Ser 2019;1168:22095. https://doi.org/10.1088/1742-6596/1168/2/022095.
31. Xu LX. A dynamic model to predict the number of pins to transmit load in a cycloidal reducer with assembling clearance. Proc Inst Mech Eng C J Mech Eng Sci 2019;233:4247–69. https://doi.org/10.1177/0954406218809732.
32. Xu LX, Chen BK, Li CY. Dynamic modelling and contact analysis of bearing-cycloid-pinwheel transmission mechanisms used in joint rotate vector reducers. Mech Mach Theory 2019;137:432–58. https://doi.org/10.1016/j.mechmachtheory.2019.03.035.
33. Król R. Analysis of the backlash in the single stage cycloidal gearbox. Archive of Mechanical Engineering 2022;69:693–711. https://doi.org/10.24425/ame.2022.141521.
34. Csobán A. Impacts of a profile failure of the cycloidal drive of a planetary gear on transmission gear. Lubricants 2021;9. https://doi.org/10.3390/lubricants9070071.
35. Kostić N, Blagojević M, Petrović N, Matejić M, Marjanović N. Determination of real clearances between cycloidal speed reducer elements by the application of heuristic optimization. Transactions of Famena 2018;42:15–26. https://doi.org/10.21278/TOF.42102.
36. Blagojević M, Matejić M, Kostić N. Dynamic behaviour of a two-stage cycloidal speed reducer of a new design concept. Tehnicki Vjesnik 2018;25:291–8. https://doi.org/10.17559/TV-20160530144431.
37. Wikło M, Krzysztof O, Krzysztof K, Król K, Komorska I. Experimental vibration test of the cycloidal gearbox with different working conditions. Vibroengineering Procedia, vol. 13, EXTRICA; 2017, p. 24–7. https://doi.org/10.21595/vp.2017.19073.
38. Hsieh CF, Jian WS. The effect on dynamics of using various transmission designs for two-stage cycloidal speed reducers. Proc Inst Mech Eng C J Mech Eng Sci 2016;230:665–81. https://doi.org/10.1177/0954406215618984.
39. Xuan L, Xie C, Guan T, Lei L, Jiang H. Research on dynamic modeling and simulation verification of a new type of FT pin-cycloid transmission. Proc Inst Mech Eng C J Mech Eng Sci 2019;233:6276–88. https://doi.org/10.1177/0954406219861999.
40. Yang R, An Z. Theoretical calculation and experimental verification of the elastic angle of a cycloid ball planetary transmission based on the axial pretightening force. Advances in Mechanical Engineering 2017;9:1–17. https://doi.org/10.1177/1687814017734112.
41. Król R. Software for the cycloidal gearbox multibody dynamics analysis, implemented in Fortran. (Purpose: presentation of the results in the scientific article) 2022. https://doi.org/10.5281/ZENODO.7221146.
42. Nikravesh PE. Planar Multibody Dynamics. 2018. https://doi.org/10.1201/b22302.
43. Nikravesh PE. Planar multibody dynamics: Formulation, programming and applications. 2007.
44. Flores P, Lankarani HM. Contact Force Models for Multibody Dynamics. vol. 226. Cham: Springer International Publishing; 2016. https://doi.org/10.1007/978-3-319-30897-5.
45. MSC Software. MSC Adams Solver Documentation n.d.
46. MSC Software. MSC Adams View Documentation. n.d.

This research utilised the MSC Software National Scientific Software License, operated by the TASK Computer Centre in Gdańsk (Poland). This license was funded by a computational grant obtained by Kazimierz Pulaski University of Technology and Humanities in Radom, Poland.

Roman Król: https://orcid.org/0000-0002-6279-9562

Kazimierz Król: https://orcid.org/0000-0002-8131-468X